Article

Exo-chirality of the α-helix

Check for updates

Jose M. Martínez-Parra[1], Rebeca Gómez-Ojea[1], Geert A. Daudey [1], Martin Calvelo [1], Hector Fernández-Caro[1], Javier Montenegro [1] & Julian Bergueiro [1]

The structure of helical polymers is dictated by the molecular chirality of their monomer units. Particularly, macromolecular helices with monomer sequence control have the potential to generate chiral topologies. In α-helical folded peptides, the sequential repetition of amino acids generates a chiral layer defined by the amino acid side chains projected outside the amide backbone. Despite being closely related to peptides' structural and functional properties, to the best of our knowledge, a general exo-helical symmetry model has not been yet described for the α-helix. Here, we perform the theoretical, computational, and spectroscopic elucidation of the α-helix principal exo-helical topologies. Non-canonical labeled amino acids are employed to spectroscopically characterize the different exo-helical topologies in solution, which precisely match the theorical prediction. Backbone-to-chromophore distance also shows the expected impact in the exo-helices' geometry and spectroscopic fingerprint. Theoretical prediction and spectroscopic validation of this exo-helical topological model provides robust experimental evidence of the chiral potential on the surface of helical peptides and outlines an entirely new structural scenario for the α-helix.

The rotation sense of helical polymers is strictly dictated by the molecular chirality of their monomer building blocks. This hierarchical chiral imposition principle has governed the design of a wide range of helical polymers, regardless of their monomer units[1–6]. By controlling the sequence of such monomers, chemical information can be topologically encoded along the helical polymer backbone[7,8]. Indeed, different homochiral monomers have been selected by evolution to generate essential helical biopolymers[9]. The sequential repetition of monomers in this type of helical backbones can generate a second layer of chirality. However, the new chiralities will no longer depend solely on the molecular structure of the monomers, but also on their sequential arrangement. Peptides can be synthesized with monomer sequence control and designed to fold into helical secondary conformations such as the α-helix. In this naturally predominant secondary structure, the amino acid side chains are projected outwards from the amide helical backbone. Thus, this helical architecture allows a virtually infinite number of three-dimensional surface topologies[10–12]. In detail, the surface topologies that emerge from repeating patterns in the amino acid sequence (*i*, *i* + *x*) define exo-helices along the

longitudinal axis of the polymer (Fig. 1). Certain topologies within this exo-helical pool can impact peptide structure and function[13,14]. Crick and others have described the importance of the exo-helical topology resulting from the (*i*, *i* + 7) repeat in the assembly of coiled coils by the leucine zipper and the knobs into holes models[15–19]. Implicit in Crick's seminal studies, and shown in subsequent work by other authors, the impact of the exo-chirality of the α-helix has been recognized in a number of intriguing peptide assemblies[20–25]. This second layer of chiral symmetry has also been related to the chiro-selective recognition and the homochiral amplification of self-replicating coiled peptides[26].

However, despite the possible fundamental and structural implications of the different exo-helical symmetries of the α-helix, the theoretical description and experimental validation of such a general topological scenario have not been reported yet. In this work, we theoretically define and experimentally confirm the general structural model for the primary topologies emerging from the (*i*, *i* + *x*) amino acid repetition patterns in the α-helix. We observed an accurate spectroscopic chiral response that confirms the exo-helical

[1]Departamento de Química Orgánica, Centro Singular de Investigación en Química Bioláxica e Materiais Moleculares (CiQUS), Universidade de Santiago de Compostela, 15705 Santiago de Compostela, Spain. e-mail: javier.montenegro@usc.es; julian.bergueiro.alvarez@usc.es
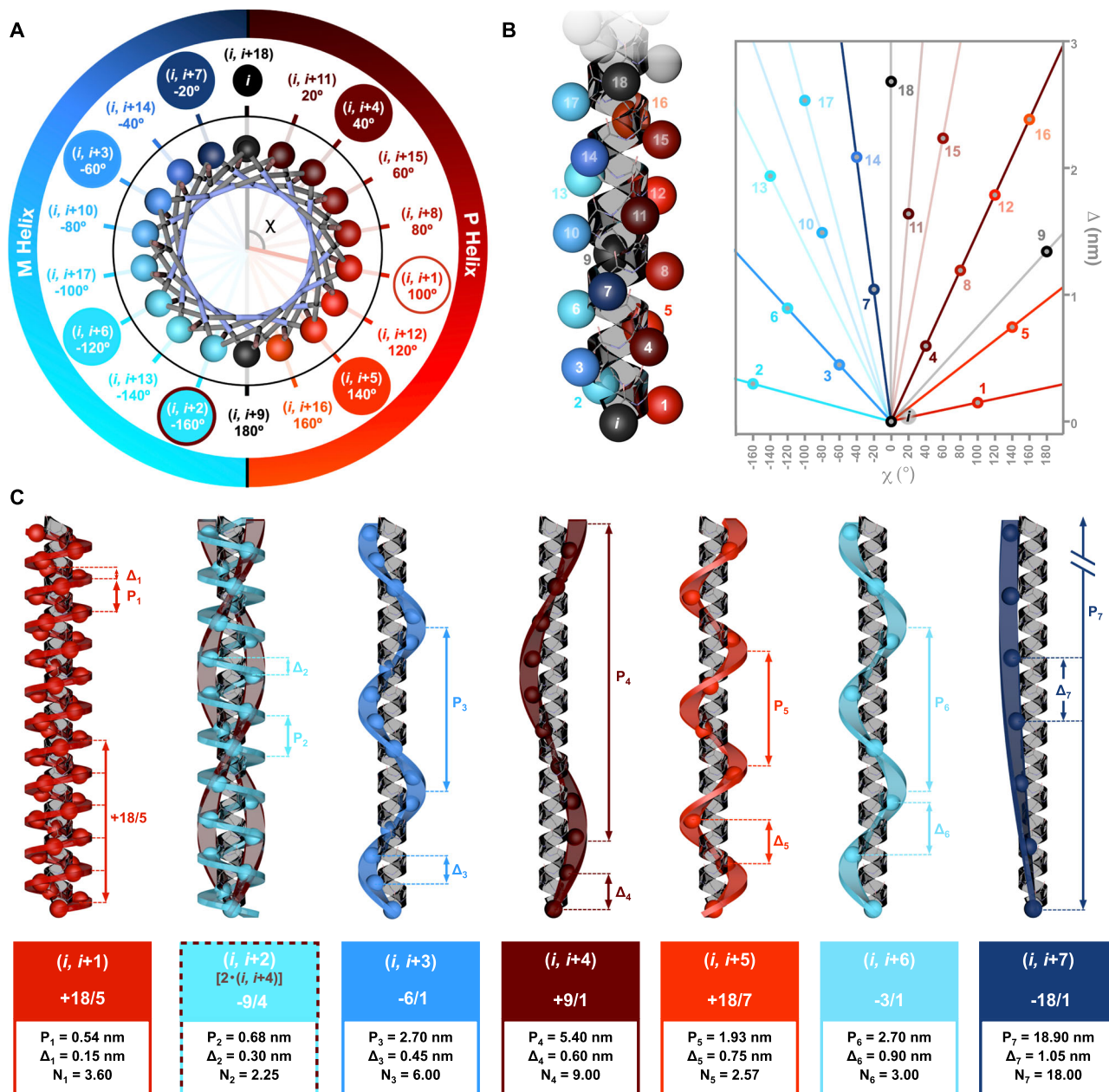
Fig. 1 | Exo-helical symmetries of the α-helix defined by amino acid periodical repetition patterns. A Helical wheel with $\Omega = 100°$. Exo-helical rotational angles (χ) for the first 18 repetition patterns ($i, i+x$) are shown. P exo-helices in shades of red on the right half of the wheel and M exo-helices in shades of blue on the left wheel side. **B** Representation of the helical symmetries for the α-helix first 18 residues in a χ vs. Δ plot. **C** Side view of the exo-helices generated by the first seven repetition patterns ($x = 1$–7 for ($i, i+x$)). Helical types are displayed for all cases together with the calculated P, Δ, and number of units per helical turn (N). The first repetition pattern ($i, i+1$) describes an exo-helix (dark red) with the same structural parameters as the α-helix. For ($i, i+2$) pattern, the pattern helix is shown in light blue and as a double ($i, i+4$) helix in dark brown. Exo-helices are expressed by the formula $\pm R/T$, where ($\pm$) defines the right (+, P) or left (−, M) helical sense. R indicates the total number of helical monomer repeats per turn, and T the total number of turns.

arrangement of the lateral side chains of sequentially repeated amino acids. These results establish the general exo-helical symmetry model for the α-helix and provide valuable information for the future spectroscopic interpretation and design of synthetic peptide foldamers and helical biocompatible materials.

Results and discussion

An undistorted α-helix architecture displays backbone azimuthal rotational angles (Ω) of 100° (Eq. (S1))[27]. Over this helical scaffold, the side chains of periodically repeated amino acids ($i, i+x$) generate a family of helical topologies on the surface of the α-helix. The projection angle established between consecutive side chains of the exo-

helical pattern can be defined as the exo-helical torsion angle (χ) (Fig. 1A). This χ angle is solely dependent on Ω and the number of residues (x) in the pattern ($i, i+x$) as defined by Eq. (S2). Thus, χ values for every possible pattern constitute a distribution of even angles separated by 20° when displayed in a helical wheel with full rotation at ($i, i+18$) ($\chi = 0°$, Fig. 1A). Positive χ angles −right half of the helical wheel− describe right-handed (P) helices, whereas negative χ−left half of the helical wheel−define left-handed (M) helices (Fig. 1A). All resulting exo-helices can be conveniently grouped in helical symmetry families as shown in the χ vs. rise (Δ) plot (Fig. 1B). Apart from χ, exo-helical pitch (P), Δ, and number of monomers per turn (N) are needed to precisely define each exo-helix (Fig. 1C, see ($i, i+1$)).
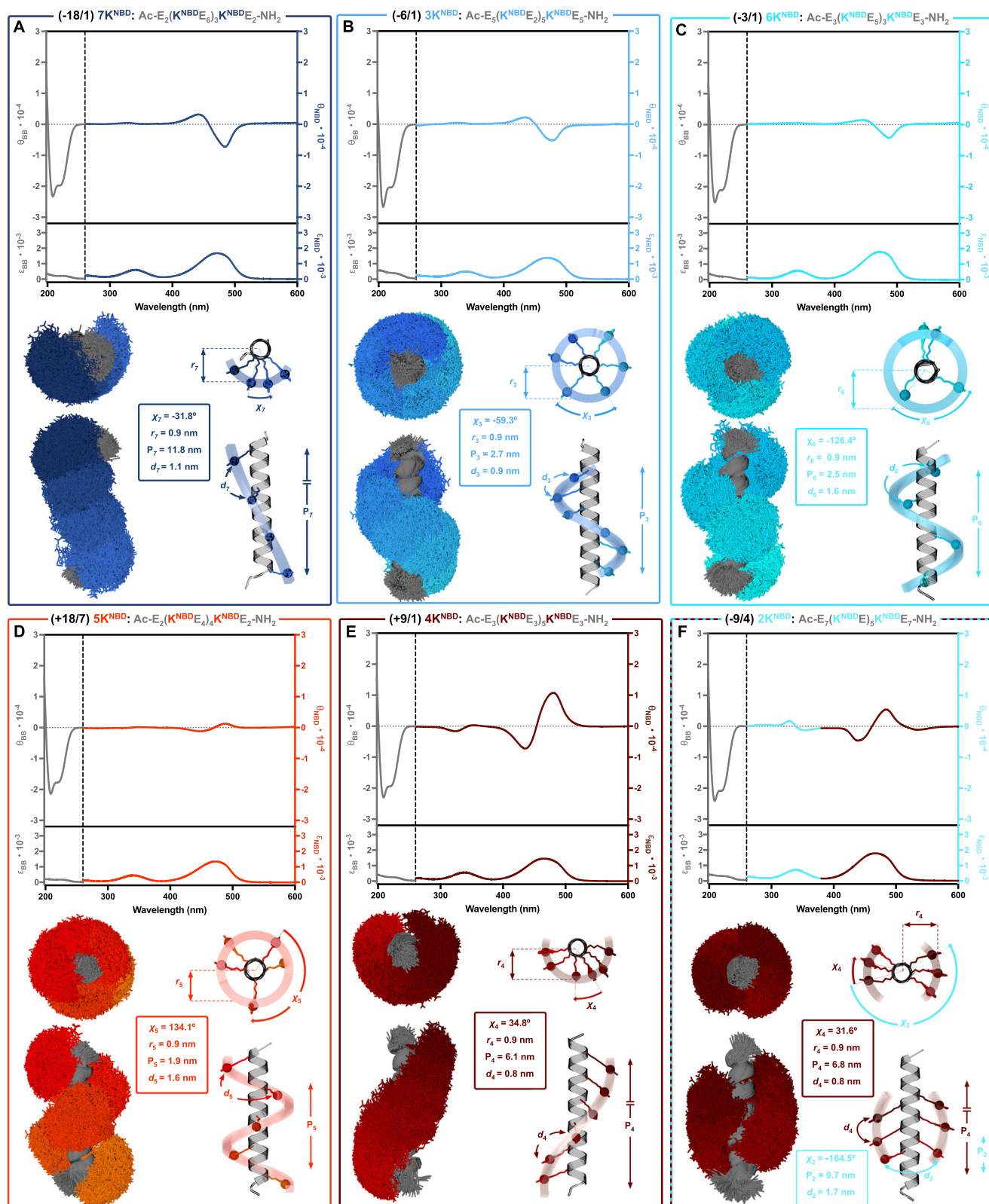
Fig. 2 | CD spectra and MD simulated averaged structures of the first six patterns (x = 2−7). For all sequences (*M*-helices: **A** 7K^{NBD}, **B** 3K^{NBD}, and **C** 6K^{NBD} top row; *P*-helices: **D** 5K^{NBD}, **E** 4K^{NBD}, and **F** 2K^{NBD} bottom row): CD and UV−Vis spectra (top box). Zenithal and lateral views of the superposition of the structures in the trajectory of the MD simulation (one structure every 500 ns, backbone is represented as a gray cartoon and K^{NBD} residues in color shades (bottom-left box). Zenithal and lateral views of the MD simulation averaged structure and the NBD centers of mass together with the exo-helical representation (bottom-right box). Structural parameters of the exo-helix (χ, r, P, and d) from the averaged structure are denoted. The calculated rotational angle of the oligo(glutamic acid) backbone (Ω) was close to the ideal value (99°), confirming the correct folding of the calculated α-helix core for all cases. θ_{BB} and θ_{NBD} expressed in deg × cm^2 × dmol^{-1}. ε_{BB} and ε_{NBD} expressed in cm^2 × dmol^{-1}.

All geometrical parameters can be calculated for any repetition pattern by simple equations (Eqs. (S3)–(5) and SI Table 1). The possible exo-helices can be predicted by the general helical symmetry model[7]. In this model, a helical symmetry group originates when the number of amino acids from a repetition pattern (x) is a prime number (Fig. 1B, C, SI Table 1, and SI Fig. 1). Exo-helices generated when x is a composite number are included in their related prime symmetry—e.g., exo-helices formed by $(i, i + 3)$ and $(i, i + 6)$ patterns are both included in the same helical symmetry (Fig. 1B and SI Fig. 1). However, when χ exceeds half rotation in the helical wheel ($\chi > 180°$ or $\chi < -180°$, Fig. 1A), a secondary helical symmetry group is induced −e.g. exo-helix generated by $(i, i + 4)$ with respect to $(i, i + 2)$ (Fig. 1B, and SI Fig. 1).

Exo-helices included in the first seven group symmetries claim our attention since they have the smallest Δ values and are possibly the most relevant examples (Fig. 1C). 2/1 $(i, i + 9)$ and 1/1 $(i, i + 18)$ symmetries corresponding with χ angles of 180 and 360°, respectively, both lead to the non-helicoidal (lineal) topology. +18/5 is the origin symmetry that contains the non-prime/non-composite repetition pattern $(i, i + 1)$ and describes an exo-helix with the same structural characteristics as the α-helical backbone (Fig. 1C). Every single exo-helix can be unequivocally expressed by the formula $\pm R/T$, where $(\pm)$ defines the right $(+, P)$ or left $(-, M)$ handed helical sense, R indicates the total number of helical monomer repeats per turn, and T the total number of turns (Fig. 1C). The first prime repetition pattern $(i, i + 2)$ describes an -9/4 M-helix with an exo-helical rotational angle of −160°. Due to this short pitch (0.68 nm), this prime pattern originates a singularity. As the $i \leftrightarrow i + 4$ exo-helical residues are closer in space than $i \leftrightarrow i + 2 - C_\beta - C_\beta$ distance of 5.7 vs. 7.7 nm, respectively− thus, the $(i, i + 2)$ pattern gives rise to a double exo-helical topology formed by two homologous $(i, i + 4)$ P-helices within the symmetry group +9/1 (Fig. 1C). The repetition patterns $(i, i + 3)$ and $(i, i + 6)$ originate to two analogous M-helices: the −6/1 and the −3/1, respectively, the latter having a half number of monomers per turn ($N = 3$) and double exo-helical rotational angle ($\chi = -120°$) (Fig. 1C). The prime number repetition pattern $(i, i + 5)$ draws a unique +18/7 exo-helix with P chirality (Fig. 1C). Finally, the $(i, i + 7)$ pattern defines a −18/1 M-exo-helix with a long helical pitch and the shortest possible rotational angle between repeated side chains ($\chi = -20°$, Fig. 1C).

The observation of the non-canonical exo-helical peptide topologies has been typically hindered, in part due to the complex structural analysis of peptides in solution. An undistorted α-helical peptide scaffold, together with a suitable characterization technique, are both required. In this sense, circular dichroism (CD) continues to be one of the techniques of choice for the determination of the average peptide secondary structure in solution due to its simplicity and versatility[28]. Thus, we designed a series of peptides that allow the characterization of the different exo-helices by CD spectroscopy. An oligo(glutamic acid) was selected as the backbone since this sequence folds into a highly stable helical conformation when protonated[29]. The low molar attenuation coefficients of the aromatic chromophores in proteinogenic amino acids (i.e., Phe, Tyr, and Trp) and their significant overlap with the amide in the UV–Vis absorbance spectrum preclude their application in the spectroscopic characterization of the exo-helices[30]. Therefore, 7-nitro-1,2,3-benzoxadiazole (NBD) was selected as a suitable chromophore for the spectroscopic characterization of the exo-helical topologies produced by the first repetition patterns $(i, i + x; x = 2-7)$. NBD has a much stronger absorbance with maxima at 482 and 348 nm ($S_0 \rightarrow S_1$ and $S_0 \rightarrow S_3$ electronic transitions, respectively), which do not overlap with the amide UV trace[31,32]. In addition, the relatively small molecular size of the NBD allows multiple functionalizations of the peptide backbone without significant helix perturbation[33].

Molecular dynamic (MD) simulations of all the NBD-bearing peptide sequences (SI Table 2) were first carried out to estimate the average structural parameters. Root-mean-square deviation (RMSD) analysis of 2 ms long trajectories showed stable structures for all

peptides, which supported the calculated trajectories as representative examples of the corresponding experimental spectroscopic traces. The averaged structures and centers of mass of the individual NBD moieties were obtained considering the whole trajectory. We could observe that the calculated azimuthal angle of the protonated oligoglutamic backbone was close to 100° ($\Omega = 99.0° \pm 0.3$), which confirmed an ideal α-helical folding in all cases. Four parameters defining all exo-helices were extracted from each averaged structure: (i) distance between neighboring NBDs (d), (ii) radius of the exo-helix formed by NBD moieties (r), (iii) helical pitch of the exo-helix (P), and finally (iv) exo-helical rotational angle (χ) as the projection angle of the chromophores' centers of mass (Fig. 2 and SI Table 3).

Oligo(glutamic acid) based peptide scaffolds were synthesized through Fmoc solid-phase strategy. Orthogonally protected side chains of lysines−i.e., methyltrityl or allyloxycarbonyl protecting groups−were installed at the NBD targeted positions of the repetition patterns $(i, i + x)$ (SI section 5). N-terminal acetylation and C-amidation were used to enhance peptide folding into α-helix and avoid undesired interhelical aggregation. Chromophore insertion was performed *on resin* by selective deprotection of the orthogonal group followed by nucleophilic aromatic substitution using NBD-Cl as electrophile. All targeted NBD-peptide sequences were obtained in high purity after HPLC purification (SI section 6). UV–Vis and CD spectroscopy data of peptide solutions (-50 μM) were recorded using 2,2,2-trifluoroethanol (TFE) as a solvent to ensure the correct folding of the individual helices (SI Table 5, SI Fig. 9–14)[34,35]. CD spectra were expressed in two molar ellipticities (θ) depending on the chromophore absorption range and normalized to the number of chromophores (eq. S8): (i) one for the peptide backbone (θ_{BB}, 190–260 nm) considering the total number of amides and (ii) a second one for the exo-helix region (θ_{NBD}, 260-600 nm) considering the number of NBD moieties. The CD signal intensity in the amide region and signal intensity ratios at the two characteristic minima (222/208 nm) experimentally confirmed the nearly ideal α-helical conformation (-80% helical content) for all peptides studied (SI Table 5). Potential chiral induction interferences between α-helix backbone and the NBD were discarded with a single NBD labeled control peptide (SI Fig. 9 and SI Table 3).

As described by the model (Fig. 1), the three-dimensional arrangement of NBD lateral residues defines a rotation sense $-P$ (+) or M (−)− for each exo-helix. MD simulations outlined left-handed exo-helices for 7K^{NBD} $(i, i + 7)$, 3K^{NBD} $(i, i + 3)$, and 6K^{NBD} $(i, i + 6)$ patterns (Fig. 2A–C). The corresponding CD traces of these three patterns revealed a negative to positive exciton coupling corresponding to the NBD $S_0 \rightarrow S_1$ transition (≈460 nm). A less intense positive signal could also be observed from the $S_0 \rightarrow S_3$ NBD transition (≈330 nm). Thus, this CD footprint was assigned to the M exo-helix generated by NBD chromophores. In detail, the M-exo-helix defined by 7K^{NBD} confirmed the predicted exo-helical rotational angle with a slight deviation ($\chi_7 = -31.8°$, Fig. 2A). This exo-helix displays the NBD moieties in relatively close spatial proximity ($d_7 = 1.1$ nm), which results in a strong NBD exciton signal (Fig. 2A). The low torsional angle and tight packing of side chains of this helical topology is optimal for the establishment of side-to-side interactions between α-helices[19,36]. Since the other two M-patterns (6K^{NBD} and 3K^{NBD}) belong to the same helical symmetry group ($^1C_3$), they describe equivalent M-exo-helices with identical helical pitch (Fig. 2B and C). However, 6K^{NBD} contains half the chromophores per helical turn than 3K^{NBD}, conferring a higher rotational degree of freedom to the chromophore moieties (Fig. 2B and C). The increased rotational freedom, together with the predicted longer interchromophore distance, is reflected in the lower exciton coupling intensity of 6K^{NBD} when compared to 3K^{NBD}.

As predicted by the model, repetition patterns 5K^{NBD} $(i, i + 5)$ and 4K^{NBD} $(i, i + 4)$ showed stable right-handed exo-helices in their MD simulations, which are experimentally confirmed by the NBD exciton couplings signature inversion (positive to negative) (Fig. 2D and E). For

$5K^{NBD}$, as anticipated from its long average inter-NBD distance ($d_5 = 1.6$ nm), only a weak bathochromic exciton coupling was observable (Fig. 2D). $4K^{NBD}$ also describes a *P*-exo-helix with an exo-helical rotational angle of 34.8° and a helical pitch of 6.1 nm (Fig. 2E). The average interchromophore distance for $4K^{NBD}$ ($d_4 = 0.8$ nm) is the shortest of all investigated patterns —as could be expected due to the anatomy of the α-helix with hydrogen bonds between ($i, i + 4$) residues. Therefore, this pattern shows the highest intensity of the CD trace for the NBD $S_0 \rightarrow S_1$ transition. The more energetic transition $S_0 \rightarrow S_3$ is also sensitive to the macrochirality of the exo-helix showing a positive to negative exciton coupling. The effect of the short distance between chromophores in $4K^{NBD}$ can also be confirmed by the blue shift of the absorbance maximum in the UV−Vis spectra (Fig. 2 and SI Fig. 15C).

$2K^{NBD}$ average structure analysis confirms a significantly larger interchromophore distance $i \leftrightarrow i + 2$ ($d_2 = 1.7$ nm) when compared with four amino acids separation $i \leftrightarrow i + 4$ ($d_4 = 0.8$ nm) (Fig. 2F). As previously mentioned, considering these distances in the exciton coupling theory, the ($i, i + 4$) contribution in the CD spectra will be predominant over that of the ($i, i + 2$) pattern. Thus, $2K^{NBD}$ will be experimentally observed in CD as an exciton coupling corresponding to two ($i, i + 4$) helices, which could be confirmed by the observed positive to negative ($S_0 \rightarrow S_1$) exciton coupling (Fig. 2E and F). The slight decrease in the CD intensity of the $2K^{NBD}$ in comparison to $4K^{NBD}$ can be explained by the higher rotational degree of freedom of four terminal chromophores instead of two (Fig. 2E and F). Interestingly, the $S_0 \rightarrow S_3$ NBD transition has a transition dipole moment (tdm) perpendicular to $S_0 \rightarrow S_1$ that is more sensitive to the ($i, i + 2$) exo-helix *M*-chirality and thus displays the expected negative to positive exciton coupling.

To understand the influence of the lateral chain molecular size in the exo-helix persistency, we next stepwise reduced the alkyl chain connecting the NBD moiety with the α amino acid from L-lysine (K, $4xCH_2$) to L-ornithine (O, $3xCH_2$), L-2,4-diaminobutyric acid (B, $2xCH_2$), and finally L-2,3-diaminopropionic acid (X, $1xCH_2$). The shortening of the alkyl linker directly reduces the rotational degree of freedom of the NBDs, which affects interchromophore distance and NBD's tdm orientation persistency (Fig. 3 and SI Table 3)[37]. Since the exciton coupling intensity is directly dependent on these parameters, CD spectroscopy should accurately report on the impact of the linker length in the exo-helix spatial distribution[38].

The different repetition patterns ($i, i + x$) of the O, B, and X peptide series was thus simulated in MD experiments, synthesized, and characterized (UV−Vis, CD) analogously to the K series (SI Figs. 9−14). For all these new peptide series, the structural values of the backbone (222/208 ratio, and % α-helix in TFE) were comparable to the K series (SI table 5). The CD spectra revealed, in all cases, the same signs as the K patterns in the NBD exciton coupling, confirming the existence of similar exo-helixes in the new three series (Fig. 3A–C and SI Figs. 10–14). In the X series, the NBD's most energetic band at 230 nm overlaps with the 222 nm signal of the peptide bond, thus influencing the 222/208 ratio. The ($i, i + 4$) pattern can be used to exemplify the different structural (MD) and spectroscopic (CD) implications of the alkyl linker length reduction (Fig. 3). Shortening the linker length linearly reduced the average interchromophore distance (d) and increased the orientation persistency of the NBD $S_0 \rightarrow S_1$ tdm (Fig. 3A–F). Considering that the orientation of the individual ($S_0 \rightarrow S_1$) NBD transition dipole moments start at the NBD center of mass and are directed towards the nitrogen atom of the nitro group (red arrows in Fig. 3A–D). The chromophore's tdm orientation persistency was measured by comparing the variations of the tdm projections in the zenithal (β_1 angle) and lateral (β_2 angle) planes (Fig. 3A–F). Thus, the root mean square of the averaged β_1 and β_2 standard deviations ($RMS\sigma_\beta$) was considered to parametrize the relative chromophore orientation persistency (Fig. 3F). A high $RMS\sigma_\beta$ value was observed for the $4O^{NBD}$, which can be rationalized by the potential promiscuous interactions established between the N_{NBD}-H and the glutamic acid

carboxylate groups, which are located at the closest distance in the ornithine linker. Following the expected trend, the shortest linker (*X*) showed the highest orientation persistency. This is supported by the favorable hydrogen bond formation between the N_{NBD}-H donors and the carbonyl acceptors of the peptide backbone (N_{NBD}-H···O $= C_{(i+4)}$) (SI Fig. 16).

As dictated by the exciton coupling theory, the effect of the chromophore to backbone distance will directly influence the two above-mentioned factors and, consequently, the UV−Vis and CD traces[6]. Consistently, we could observe the hypsochromic shift of the UV−Vis maxima, being the $4X^{NBD}$ the most blue-shifted due to the shortening of d (Fig. 3G). On the other hand, the CD trace is more sensitive to the magnetic field, as can be observed from the exponential increase of the NBD exciton coupling intensity with the chromophore orientation persistency (Fig. 3H). This trend was observed for all repetition patterns (SI Fig. 15), with the shortest linker (X series) being in all cases the most persistent in the tdm orientation and CD signal, thereby precisely matching the proposed topological model. Therefore, this observation confirms that the persistency of the exo-helix is dependent on the degree of freedom of the lateral chain. This linker length and the possible interactions of the exo-chiral pendant with the α-helix backbone can enhance the stability of certain conformations of the chromophore pendant, which will then influence the exo-helix spatial persistency. Naturally, the strength of exo-helical interactions and the function of these chiral topologies will be related to this persistence.

In conclusion, we introduce and experimentally demonstrate a general model for the exo-helical topologies of the α-helix secondary structure. A collection of oligo(glutamic acid) peptide scaffolds equipped with NBD chromophores at patterned positions were designed, simulated, synthesized, and spectroscopically characterized. The different repetition patterns ($i, i + x$) showed CD exciton couplings that consistently correlated in sign and intensity with the structural characteristics of the predicted exo-helices and their MD-simulated averaged structures. Spectroscopic elucidation of the topological model by varying the exo-helical linker length precisely matched the interchromophore distances and chromophore orientation persistency calculated by MD simulations with the exciton coupling theory. The chiral model herein proposed and spectroscopically validated confirms the α-helix potential to define different exo-helical chiral symmetries through repetition patterns in the amino acid sequence. At the present time, the future applications of the here-described exo-chiral model of the α-helix remain to be explored. However, the exo-chiral topologies of the α-helix have the potential to open the design of peptide non-canonical assemblies with multiple low-energy states, which can be found in certain functional proteins[39,40]. Moreover, we foresee that analogous exo-helical frameworks will be possible for any other helical peptide motifs, such as the 3_{10} helix, the π-helix, and related foldamers. In addition, we expect that the exo-helical model of the α-helix will assist in the future design of non-canonical folding motifs, the synthesis of homochiral peptide replicators, and the development of new stimuli-responsive helical polymers and biocompatible sensors of chirality.

Methods

All experimental details, which include all details of synthesis and characterization of all peptide series, including, UV−Vis and CD spectroscopies, MS and MD simulations details are provided in the Supplementary Information

Peptide synthesis

Solid-phase peptide syntheses (SPPS) were performed using a microwave-assisted CEM Liberty Blue automated peptide synthesizer. Reverse phase ultra-high-performance liquid chromatography coupled with mass spectrometry (UHPLC−MS) analyses were carried out
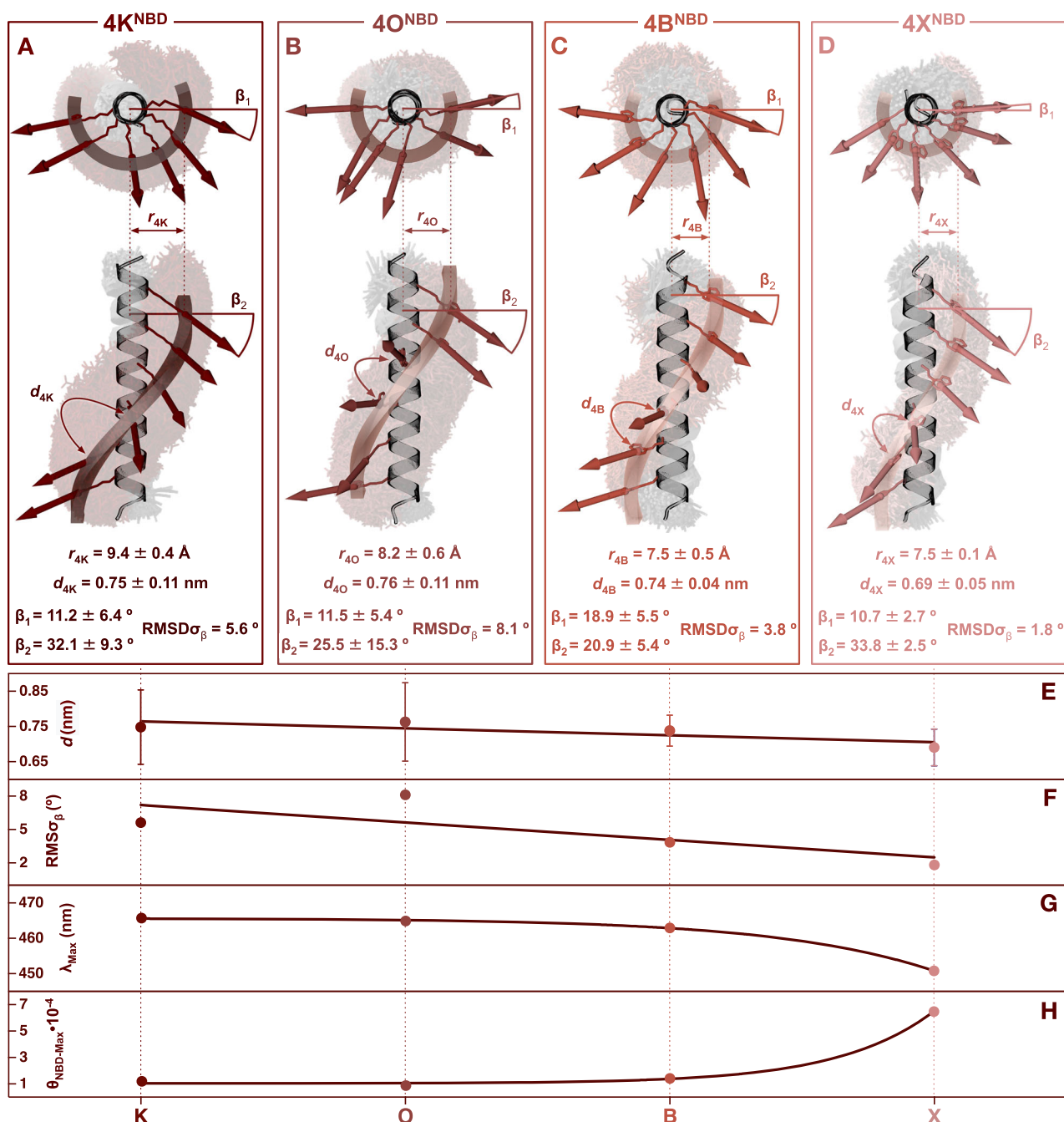
Fig. 3 | Influence of the linker length (K (CH₂)₄, O (CH₂)₃, B (CH₂)₂, and X CH₂) in the interchromophore distance and transition dipole moment orientation and its observation in CD and UV–Vis spectra for the (i, i + 4) repetition pattern. Exo-helical radii (r), interchromophore distance (d), and transition dipolar moment deviation angles (β₁ and β₂) represented in the MD simulation averaged structure output of 4K^{NBD} (**A**), 4O^{NBD} (**B**), 4B^{NBD} (**C**), and 4X^{NBD} (**D**). Interchromophore distance (d) (**E**), root mean square of the β₁ and β₂ standard deviations (RMSσ$_β$) (**F**), wavelength for NBD S₀ → S₁ transition maxima in UV–Vis (**G**), and CD NBD exciton coupling intensity at 485 nm (**H**) versus linker length. CD maxima expressed in deg × cm² × dmol^{-1}.

on an Agilent Technologies 1260 Infinity II equipped with a 6120 Quadrupole system and an Agilent SB-C18 column. Peptides were eluted with Solvent A:Solvent B gradients from 95:5 to 25:75 in a 15 min method (Solvent A: H_2O with 0.1% TFA; Solvent B: ACN with 0.1% TFA). Negative electrospray ionization mass spectrometry (ESI-MS) spectra were recorded on a Bruker Amazon SL mass spectrometer and are reported as mass-to-charge ratio (m/z). High-resolution mass determinations (HR-MS observed mass) using negative ESI-Flow injection analysis-Time of flight-MS (ESI-FIA-ToF-MS) were performed on a Bruker MicroToF mass spectrometer and are reported as a mass-to-charge ratio (m/z). Preparative reverse-phase high-performance liquid

chromatography (HPLC) purification was carried out on a Shimadzu Nexera LC20-AP equipped with a quaternary pump and an Agilent Eclipse XDB-C18 column. Semipreparative gel permeation chromatography (GPC) purification was carried out on the same instrument with a Phenomenex Shodex SB-806MHQ column. Freeze-drying steps were performed on a BUCHI Lyovapor L-300 lyophilizer.

Peptide spectroscopic characterization
Final concentrations of NBD-labeled peptides were measured by ultraviolet–visible (UV–Vis) spectroscopy on a Biochrom Libra UV/Vis S60 spectrophotometer. Full UV–Vis spectra from peptides were

recorded on a Varian-100 UV–Vis spectrophotometer. Circular dichroism (CD) measurements were performed on a Jasco J-710 CD spectrometer equipped with a NESLAB RTE-111 circulation bath.

Molecular dynamics simulations

Initial peptide geometries were obtained using Spartan. To guarantee an ideal α-helical geometry, f and y angles were selected to be −57° and −48°, respectively. The non-canonical amino acids were placed in position by replacing the lateral chains with an NBD moiety at the designed positions. Finally, the peptide N-terminus and C-terminus were capped with acetyl and amide groups respecting the backbone dihedral angles. Peptides were placed in a simulation box with a minimum distance of 10 Å from the edges of the box, and they were solvated with TFE. No ions were added due to the neutral charge of the peptide. The parameters of the Gromos 54a7 force field were selected for the standard amino acids and the ATB-server was used for the parametrization of the non-standard amino acids. We utilize the ATB given parameters without further QM calculation. SPC was chosen as the solvent model, whereas the parameters of TFE were also obtained from the ATB-server. After building the initial systems, they were minimized after 5000 steps using the steepest-descent algorithm and equilibrated towards an MD simulation during 1 ns using a time step of 2 fs applying position restraints of 1000 kJ/mol nm^2 to all non-hydrogen atoms of the protein. Then, unrestricted MD simulations were carried out during 2 µs using a time step of 2 fs. All simulations have been carried out at 298 K and 1 bar, using the V-rescale thermostat and the isotropic Parrinello–Rahman barostat. The LINCS algorithm was used for constraining all bonds. For treating the long-range electrostatic interactions, the particle mesh Ewald (PME) method with a cut-off of 1.0 nm was chosen. The Van der Waals interactions were calculated within a radius of 1.0 nm. All calculations, including the analysis of the trajectories, have been carried out with the software package Gromacs 2018.3 using the CESGA supercomputer. Averaged structures were obtained with Gromacs 2018.3 native command (gmx cluster -av) with a time step of 0.2 ns and a cutoff value of 0.5 nm, obtaining a single structure for all analyzed sequences. Structural analyses of backbone and side chain chromophore parameters were performed with Gromacs ("gmx make_ndx" and "gmx helix" commands), pymol (for the calculation of center of mases and represented as a pseudo-atom), and R packages Rpdb for distances between center of mases and Bio 3D for dihedral torsional angles. All other parameters were calculated from the previous ones.

Data availability

The MD simulation, MS, UV, and CD data generated in this study have been deposited in the Zenodo database under accession code https://doi.org/10.5281/zenodo.12726884. All data are available from the corresponding authors upon request.

References

1. Yashima, E., Maeda, K., Iida, H., Furusho, Y. & Nagai, K. Helical polymers: synthesis, structures, and functions. *Chem. Rev.* **109**, 6102–6211 (2009).
2. Arias, S., Freire, F., Calderón, M. & Bergueiro, J. Unexpected chirothermoresponsive behavior of helical poly(phenylacetylene)s bearing elastin-based side chains. *Angew. Chem. Int. Ed.* **56**, 11420–11425 (2017).
3. Leigh, T. & Fernandez-Trillo, P. Helical polymers for biological and medical applications. *Nat. Rev. Chem.* **4**, 291–310 (2020).
4. Magnotti, E. L. et al. Self-assembly of an α-helical peptide into a crystalline two-dimensional nanoporous framework. *J. Am. Chem. Soc.* **138**, 16274–16282 (2016).
5. De, S. et al. Designing cooperatively folded abiotic uni- and multimolecular helix bundles. *Nat. Chem.* **10**, 51–57 (2018).
6. Dietzsch, J., Bialas, D., Bandorf, J., Würthner, F. & Höbartner, C. Tuning exciton coupling of merocyanine nucleoside dimers by RNA, DNA and GNA double helix conformations. *Angew. Chem. Int Ed.* **61**, e202116783 (2022).
7. Wang, F., Gnewou, O., Solemanifar, A., Conticello, V. P. & Egelman, E. H. Cryo-EM of helical polymers. *Chem. Rev.* **122**, 14055–14065 (2022).
8. Gellman, S. H. Foldamers: a manifesto. *Acc. Chem. Res.* **31**, 173–180 (1998).
9. Sallembien, Q., Bouteiller, L., Crassous, J. & Raynal, M. Possible chemical and physical scenarios towards biological homochirality. *Chem. Soc. Rev.* **51**, 3436–3476 (2022).
10. Haack, T. et al. Surface recognition and helix stabilization of a tetraaspartate peptide by shape and electrostatic complementarity of an artificial receptor. *J. Am. Chem. Soc.* **121**, 11813–11820 (1999).
11. Jayatunga, M. K. P., Thompson, S. & Hamilton, A. D. α-Helix mimetics: outwards and upwards. *Bioorg. Med. Chem. Lett.* **24**, 717–724 (2014).
12. Ljubetič, A., Gradišar, H. & Jerala, R. Advances in design of protein folds and assemblies. *Curr. Opin. Chem. Biol.* **40**, 65–71 (2017).
13. Miller, J. G., Hughes, S. A., Modlin, C. & Conticello, V. P. Structures of synthetic helical filaments and tubes based on peptide and peptido-mimetic polymers. *Q. Rev. Biophys.* **55**, e2 (2022).
14. Daugherty, D. L. & Gellman, S. H. A fluorescence assay for leucine zipper dimerization: avoiding unintended consequences of fluorophore attachment. *J. Am. Chem. Soc.* **121**, 4325–4333 (1999).
15. Crick, F. H. C. The packing of -helices: simple coiled-coils. *Acta Crystallogr.* **6**, 689–697 (1953).
16. Pelay-Gimeno, M., Glas, A., Koch, O. & Grossmann, T. N. Structure-based design of inhibitors of protein–protein interactions: mimicking peptide binding epitopes. *Angew. Chem. Int. Ed. Engl.* **54**, 8896–8927 (2015).
17. Boyle, A. L. & Woolfson, D. N. De novo designed peptides for biological applications. *Chem. Soc. Rev.* **40**, 4295–4306 (2011).
18. Ljubetič, A. et al. Design of coiled-coil protein-origami cages that self-assemble in vitro and in vivo. *Nat. Biotechnol.* **35**, 1094–1101 (2017).
19. Walters, R. F. S. & DeGrado, W. F. Helix-packing motifs in membrane proteins. *Proc. Natl Acad. Sci. USA.* **103**, 13658–13663 (2006).
20. Todd, A. P. & Millhauser, G. L. ESR spectra reflect local and global mobility in a short spin-labeled peptide throughout the .alpha.-helix .fwdarw. coil transition. *Biochemistry* **30**, 5515–5523 (1991).
21. Fiori, W. R., Miick, S. M. & Millhauser, G. L. Increasing sequence length favors .alpha.-helix over 310-helix in alanine-based peptides: evidence for a length-dependent structural transition. *Biochemistry* **32**, 11957–11962 (1993).
22. Bolin, K. A. & Millhauser, G. L. α and 3_{10}: The Split Personality of Polypeptide Helices. *Acc. Chem. Res.* **32**, 1027–1033 (1999).
23. Alvarez, B. H. et al. A transition from strong right-handed to canonical left-handed supercoiling in a conserved coiled-coil segment of trimeric autotransporter adhesins. *J. Struct. Biol.* **170**, 236–245 (2010).
24. Schmidt, N. W., Grigoryan, G. & DeGrado, W. F. The accommodation index measures the perturbation associated with insertions and deletions in coiled-coils: Application to understand signaling in histidine kinases. *Prot. Sci.* **26**, 414–435 (2017).
25. Hutchins, G. H. et al. An expandable, modular de novo protein platform for precision redox engineering. *Proc. Natl. Acad. Sci. USA* **120**, e2306046120 (2023).
26. Saghatelian, A., Yokobayashi, Y., Soltani, K. & Ghadiri, M. R. A chiroselective peptide replicator. *Nature* **409**, 797–801 (2001).
27. Richardson, J. S. The anatomy and taxonomy of protein structure. *Adv. Protein Chem.* **34**, 167–339 (1981).
28. Rogers, D. M. et al. Electronic circular dichroism spectroscopy of proteins. *Chem* **5**, 2751–2774 (2019).

29. Finke, J. M., Jennings, P. A., Lee, J. C., Onuchic, J. N. & Winkler, J. R. Equilibrium unfolding of the poly(glutamic acid)20 helix. *Biopolymers* **86**, 193–211 (2007).
30. Balestrieri, C. et al. Second-derivative spectroscopy of proteins. *Eur. J. Biochem* **90**, 433–440 (1978).
31. Amaro, M., Filipe, H. A. L., Ramalho, J. P. P., Hof, M. & Loura, L. M. S. Fluorescence of nitrobenzoxadiazole (NBD)-labeled lipids in model membranes is connected not to lipid mobility but to probe location. *Phys. Chem. Chem. Phys.* **18**, 7042–7054 (2015).
32. Benson, S. et al. SCOTfluors: Small, Conjugatable, Orthogonal, and Tunable fluorophores for in vivo imaging of cell metabolism. *Angew. Chem. Int. Ed.* **58**, 6911–6915 (2019).
33. Mühlberg, M., Siebertz, K. D., Schlegel, B., Schmieder, P. & Hackenberger, C. P. R. Controlled thioamide vs. amide formation in the thioacid–azide reaction under acidic aqueous conditions. *Chem. Commun.* **50**, 4603–4606 (2014).
34. Schuh, M. D. & Baldwin, M. C. α-Helix formation in melittin and β-lactoglobulin A induced by fluorinated dialcohols. *J. Phys. Chem. B* **110**, 10903–10909 (2006).
35. Luo, P. & Baldwin, R. L. Mechanism of helix induction by trifluoroethanol: a framework for extrapolating the helix-forming properties of peptides from trifluoroethanol/water mixtures back to water †. *Biochem.-us* **36**, 8413–8421 (1997).
36. Woolfson, D. N. The design of coiled-coil structures and assemblies. *Adv. Protein Chem.* **70**, 79–112 (2005).
37. Wolffs, M. et al. Helical aromatic oligoamide foldamers as organizational scaffolds for photoinduced charge transfer. *J. Am. Chem. Soc.* **131**, 4819–4829 (2009).
38. Li, Z. & Hirst, J. D. Quantitative first principles calculations of protein circular dichroism in the near-ultraviolet. *Chem. Sci.* **8**, 4318–4333 (2017).
39. Regan, L. et al. Protein design: Past, present, and future. *Biopolymers* **104**, 334–350 (2015).
40. Huang, P. S., Boyken, S. & Baker, D. The coming of age of de novo protein design. *Nature* **537**, 320–327 (2016).

Author contributions
J.B. and J.M. conceived the project and designed the experiments. J.B., J.M.M.-P., R.G-O., G.A.D., and H.F-C. carried out chemical synthesis, purification, and characterization. J.B. and M.C. performed the computational studies. J.B. and J.M. wrote the manuscript, with all other authors contributing to its final version.

Competing interests
The authors declare no competing interests.

Additional information
Supplementary information The online version contains supplementary material available at https://doi.org/10.1038/s41467-024-51072-8.

Correspondence and requests for materials should be addressed to Javier Montenegro or Julian Bergueiro.

Peer review information *Nature Communications* thanks the anonymous reviewer(s) for their contribution to the peer review of this work. A peer review file is available.

Reprints and permissions information is available at http://www.nature.com/reprints

Publisher's note Springer Nature remains neutral with regard to jurisdictional claims in published maps and institutional affiliations.